

# Observation of a Rare Earth Ion–Extractant Complex Arrested at the Oil–Water Interface During Solvent Extraction

Wei Bu,<sup>\*,†</sup> Hao Yu,<sup>†</sup> Guangming Luo,<sup>‡,§</sup> Mrinal K. Bera,<sup>†</sup> Binyang Hou,<sup>†</sup> Adam W. Schuman,<sup>†</sup> Binhu Lin,<sup>||</sup> Mati Meron,<sup>||</sup> Ivan Kuzmenko,<sup>§</sup> Mark R. Antonio,<sup>‡</sup> L. Soderholm,<sup>\*,‡</sup> and Mark L. Schlossman<sup>\*,†</sup>

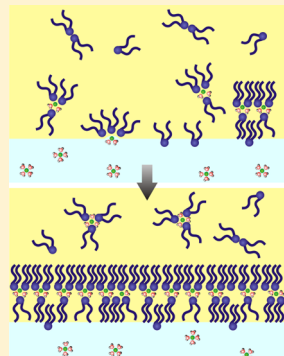
<sup>†</sup>Department of Physics, University of Illinois at Chicago, Chicago, Illinois 60607, United States

<sup>‡</sup>Chemical Sciences and Engineering Division, and <sup>§</sup>XSD, Advanced Photon Source, Argonne National Laboratory, Argonne, Illinois 60439, United States

<sup>||</sup>Center for Advanced Radiation Sources, University of Chicago, Chicago, Illinois 60637, United States

## Supporting Information

**ABSTRACT:** Selective extraction of metal ions from a complex aqueous mixture into an organic phase is used to separate toxic or radioactive metals from polluted environments and nuclear waste, as well as to produce industrially relevant metals, such as rare earth ions. Selectivity arises from the choice of an extractant amphiphile, dissolved in the organic phase, which interacts preferentially with the target metal ion. The extractant-mediated process of ion transport from an aqueous to an organic phase takes place at the aqueous–organic interface; nevertheless, little is known about the molecular mechanism of this process despite its importance. Although state-of-the-art X-ray scattering is uniquely capable of probing molecular ordering at a liquid–liquid interface with subnanometer spatial resolution, utilizing this capability to investigate interfacial dynamical processes of short temporal duration remains a challenge. We show that a temperature-driven adsorption transition can be used to turn the extraction on and off by controlling adsorption and desorption of extractants at the oil–water interface. Lowering the temperature through this transition immobilizes a supramolecular ion–extractant complex at the interface during the extraction of rare earth erbium ions. Under the conditions of these experiments, the ion–extractant complexes condense into a two-dimensional inverted bilayer, which is characterized on the molecular scale with synchrotron X-ray reflectivity and fluorescence measurements. Raising the temperature above the transition leads to Er ion extraction as a result of desorption of ion–extractant complexes from the interface into the bulk organic phase. XAFS measurements of the ion–extractant complexes in the bulk organic phase demonstrate that they are similar to the interfacial complexes.



## 1. INTRODUCTION

The transport of ions across liquid–liquid interfaces underlies a wide variety of biological, environmental, and industrial processes.<sup>1–3</sup> Although there have been studies focused on various aspects of metal–ion phase transfer, a paucity of relevant data has prohibited the development of a molecular-level understanding of events occurring at the interface. Recent advances in X-ray interface-sensitive techniques<sup>4</sup> now extend the capability to probe molecular-level speciation and organization to liquid–liquid interfaces. Herein, we apply these techniques to probe molecular-level organization at an aqueous–organic solution interface with specific relevance to solvent extraction.

Solvent extraction, an important industrial process for separating, isolating, and thus purifying metal ions, involves the transfer of a targeted species between two immiscible solution phases.<sup>5–8</sup> The process involves contact of an aqueous phase containing a mixture of ionic species with an organic phase to which the targeted metal species is to be selectively transferred by complexation with an amphiphilic extractant molecule, which serves to solubilize the metal cation in the

nonpolar phase. Until recently, the major energetic driver for this process has been thought to center on small differences in molecular energetics favoring the molecular metal–extractant complex.<sup>9</sup> New evidence is changing this perspective, suggesting instead that efficient metal extraction processes may involve the formation of extractant-based clusters in the organic phase.<sup>10,11</sup> Described in terms of reverse micelles, these clusters are comprised of extractants that self-organize. Critical to, but missing from this model, is knowledge of how the micelles are formed and how the targeted ions become enclosed in these supramolecular structures. Our X-ray studies provide the basis for a molecular-level understanding of interactions and organization at the liquid–liquid interface through evidence of an interfacial route to such supramolecular structures. Although this work focuses on a system of relevance to solvent extraction, the results provide new insight into molecular-level processes at liquid–liquid interfaces.

**Received:** June 6, 2014

**Revised:** August 18, 2014

**Published:** August 19, 2014

Building on studies of erbium in bulk water and at the water–vapor interface,<sup>12,13</sup> we formed liquid–liquid interfaces between aqueous solutions of ErCl<sub>3</sub> or ErBr<sub>3</sub> and immiscible organic solutions of dihexadecyl phosphate (DHDP) in dodecane as a model system for a typical solvent extraction system. The phosphate headgroup of DHDP, which complexes with Er<sup>3+</sup>, is present in industrial acidic organo-phosphorus extractants,<sup>3</sup> such as di(2-ethylhexyl) phosphate and di-*n*-hexyl phosphate. Although not an industrial extractant itself, the amphiphilic nature of DHDP allowed us to slow interfacial kinetics sufficiently to place the dodecane–water interface in a long-lived (>1 day) condensed state of supramolecular ion–extractant complexes. Its structure was then determined with X-ray reflectivity and fluorescence measurements. Supramolecular complexes in the bulk organic phase, whose coordination of ions and extractants is consistent with the measured interfacial structure, were subsequently observed after extraction with X-ray absorption fine structure (XAFS) measurements.

## 2. MATERIALS AND METHODS

**Materials and Preparation.** The dodecane–water interface was selected for this study because of its use in industrial applications of solvent extraction. Dodecane purchased from Sigma-Aldrich (>99%) was further purified by passing it six times through activated alumina in a chromatography column. Dihexadecyl phosphate (DHDP, >98% purity from Sigma-Aldrich) was purified by recrystallizing it twice from chloroform. Erbium bromide hydrate (ErBr<sub>3</sub>·9H<sub>2</sub>O; >99.999%) and erbium chloride hexahydrate (ErCl<sub>3</sub>·6H<sub>2</sub>O; >99.999%) were purchased from Sigma-Aldrich and Alfa-Aesar, respectively, and further purified by shaking concentrated solutions (0.75 M for ErBr<sub>3</sub> and 1 M for ErCl<sub>3</sub>) in a slow rocker and filtering them through Omnipore membrane paper to remove surface-active impurities. Further purification occurred by placing the solutions in contact with purified dodecane in a separation funnel for several hours, then draining the lower fraction that is not in contact with the interface from the funnel. This was used as a stock solution for preparing lower concentration aqueous solutions. Ultrapure water from a Nano pure UV Barnstead system was used for all aqueous solutions. Hydrobromic acid (Optima) and hydrochloric acid (Optima) from Fisher Scientific were used to adjust the pH values of ErBr<sub>3</sub> and ErCl<sub>3</sub> solutions, respectively. The chosen value of pH, 2.5, was used to mimic the low-pH commonly used in industrial solvent extraction that utilizes organo-phosphorus extractants.<sup>14</sup> The concentrations of the ErBr<sub>3</sub> ( $5 \times 10^{-7}$  M), ErCl<sub>3</sub> (1 to ~3  $\times 10^{-7}$  M), and DHDP ( $10^{-4}$  M) solutions are low to avoid precipitation. The  $10^{-4}$  M DHDP dodecane solution was prepared at 50 °C due to its low solubility at room temperature, then cooled to the desired temperature. In the experiments, the DHDP solutions were always below the solubility limit. Dodecane–water interfaces (2.2:1 volume ratio) were studied by X-rays in a specially designed Teflon cell<sup>15</sup> placed in a single stage, custom-designed thermostat for temperature control ( $\pm 0.03$  °C).

**Interfacial Tension Measurements.** Equilibrated interfacial tensions were measured with the Wilhelmy plate method. The aqueous phase completely wets the Wilhelmy plate, made of chromatography paper, and pulls it downward. The plate is attached to an electronic balance via a platinum wire, which measures the force exerted on the plate. The interfacial tension is simply this force divided by the wetted perimeter of the Wilhelmy plate. The samples were contained in a temperature-

controlled glass dish (1:1 volume ratio dodecane:water) whose temperature was varied from 25 to 50 °C. The tension is monitored as a function of time to ensure equilibration, which takes approximately 1.5 h for each data point.

**Brewster Angle Microscopy.** A custom Brewster angle microscope was used to image monolayers at the liquid–liquid interface.<sup>16</sup> The reflection of p-polarized light at the Brewster angle would be extinguished from an ideal, step-function dielectric interface, but deviations from ideality due to the presence of, for example, interfacial domains of extractants, lead to weak reflections that are used to image the interfacial phase morphology. The diffraction limit of the microscope is 3 μm in the plane of the interface. Concurrent quasi-elastic light scattering measurements of the interfacial tension were taken to determine the temperature of the adsorption transition.<sup>16</sup>

**Samples for XAFS Measurements of the Bulk Organic Phase.** Samples were prepared by placing 5 mL of 0.1, 0.5, and 1 mM ErBr<sub>3</sub> aqueous solutions (pH = 2.5, adjusted with HBr) in contact, respectively, with 5 mL of 1, 5, and 10 mM DHDP in dodecane in a glass beaker at 55 °C for over 24 h. The organic phases were then isolated for XAFS measurements. Different concentrations were studied because the higher concentration samples exhibited partial crystal precipitation with time, as a result of the low solubility of DHDP in dodecane at room temperature, with the 1 mM ErBr<sub>3</sub> sample eventually becoming a gel. The lowest concentration sample did not provide a high signal-to-noise XAFS data at high  $k$ . Nevertheless, the data remained unchanged during the precipitation process, and were also similar for samples at the three different concentrations. This suggests that data from any of the three concentration samples are representative of the extracted Er–DHDP complex. A reference sample of 22 mM ErBr<sub>3</sub> aqueous solution was also studied, whose concentration was chosen to provide a strong Er signal in the absence of DHDP.

**X-ray Beamlines.** X-ray reflectivity and X-ray fluorescence near total reflection (XFNTR) data were measured at the Advanced Photon Source (Argonne National Laboratory, IL) beamlines 15-ID and 9-ID using 20.000 keV X-rays with techniques described elsewhere.<sup>4,15,17</sup> Erbium L3-edge (8.358 keV) EXAFS data were acquired on bending magnet station 12-BM-B at the Advanced Photon Source (Argonne National Laboratory, IL).

**X-ray Reflectivity.** X-ray reflectivity data were fit to a model functional form to determine the electron density profile  $\rho(z)$  along the direction  $z$  perpendicular to the interface, but averaged over the  $x$ – $y$  plane of the interface. The model is a sum of error functions:

$$\rho(z) = \frac{1}{2} \sum_{i=0}^{N-1} \text{erf}\left(\frac{z - z_i}{\sqrt{2}\sigma}\right)(\rho_i - \rho_{i+1}) + \frac{\rho_0 + \rho_N}{2} \quad (1)$$

where  $\text{erf}(z) = (2/\sqrt{\pi}) \int_0^z e^{-t^2} dt$ ;  $N$  is the number of internal interfaces;  $\rho_i$  is the electron density of the  $i$ th slab where  $\rho_0 = \rho_{\text{aq}}$  and  $\rho_N = \rho_{\text{dodecane}}$  are the electron densities of the bulk aqueous and organic phases;  $z_i$  is the position of the  $i$ th interface;  $\sigma$  is the interfacial roughness. The thickness of the  $i$ th slab,  $d_i$ , is defined as  $|z_i - z_{i-1}|$ . X-ray reflectivity was calculated from the discretized density profile determined from eq 1 by use of the Parratt formalism.<sup>18</sup> Nonlinear least-squares fitting was used to determine the minimum number,  $N - 1$ , of internal slabs that were required to fit the X-ray reflectivity data, where the minimum number of internal slabs is defined by that

number for which an additional slab does not improve the quality of the fit significantly.

The interfacial roughness  $\sigma$  can be calculated from capillary wave theory:<sup>4</sup>

$$\sigma^2 = \frac{k_B T}{2\pi\gamma} \ln \frac{4}{Q_z \Delta\beta r} \quad (2)$$

where  $k_B$  is the Boltzmann constant,  $T$  is the temperature in Kelvin,  $\gamma$  is the interfacial tension,  $\Delta\beta$  is the detector acceptance, and  $r$  is the average molecular radius. Substitution of  $T = 301$  K,  $Q_z = 0.45 \text{ \AA}^{-1}$  (maximum value),  $\Delta\beta = 0.67$  and 0.58 mrad, respectively, for the samples with pure water and  $\text{ErBr}_3$  aqueous solutions, and  $r = 4.8 \text{ \AA}$  (average distance between DHDHP molecules) into eq 2, together with the measured interfacial tension, yields  $\sigma = 4.8 \pm 0.2 \text{ \AA}$  and  $\sigma = 3.8 \pm 0.1 \text{ \AA}$ , respectively, for samples with pure water and  $\text{ErBr}_3$  aqueous solutions.

X-ray reflectivity measurements were normalized to the Fresnel reflectivity  $R_F(Q_z)$  that was calculated for a theoretical liquid–liquid interface whose electron density varies as a step-function between the values of the bulk liquid electron densities.<sup>4</sup>

**X-ray Fluorescence Near Total Reflection (XFNTR).** The total fluorescence intensity  $I = I_B + I_I + I_b$  includes three contributions: bulk  $I_B$ , interface  $I_I$ , and background  $I_b$ . The interfacial term is negligible for a reference sample without extractant, that is, the interface between dodecane and a 0.1 M  $\text{ErBr}_3$  aqueous solution. Assuming that the  $\text{Er}^{3+}$  concentration is uniform everywhere in the aqueous phase of the reference sample, the intensity is given by  $I = I_B + I_b = C\rho_{\text{bulk}}TS + I_b$ , where  $C$  is a scale factor that accounts for the effect of the sample and scattering geometry,  $\rho_{\text{bulk}}$  is the ion bulk concentration,  $T$  is the Fresnel transmission, and  $S$  is the integration of X-ray intensity over the effective area.<sup>15</sup> The background term  $I_b$  is generated by secondary scattering from the top phase, which could dominate the signal at low  $Q_z$  but vanishes for a dilute-ion solution.<sup>15</sup> The best fit to a reference sample (see Figure S1 in the Supporting Information) yielded the scale factor  $C = 7.48 \pm 0.12 \times 10^{-7} \text{ \AA}$ .

### 3. RESULTS AND ANALYSIS

#### Controlling Extractant Adsorption at the Interface.

The molecular processes to form ion–extractant complexes and transport them across the oil–water interface occur faster than the fraction of an hour to several hours required to characterize these complexes by X-ray surface scattering and fluorescence techniques. Controlling the interaction of extractants with the interface allowed us to arrest the extraction process and immobilize ion–extractant complexes at the interface for many hours. This control was achieved through an adsorption transition realized by the choice of extractant.

Interfacial tension and X-ray surface scattering measurements have previously demonstrated that single-chain nonionic surfactants dissolved in alkane liquids will adsorb onto the alkane–water liquid–liquid interface as the temperature is lowered through a first-order adsorption transition.<sup>19–21</sup> At temperatures below the transition, surfactants form a condensed monolayer on the interface; above the transition, a dilute concentration of surfactants occupies the interface. Adjusting the temperature from above to below the transition temperature  $T_0$  brings surfactants from the oil phase, which serves as a reservoir of surfactants, to the interface to form a

condensed layer. Surfactants desorb from the interface into the bulk oil phase when the temperature is raised above  $T_0$ . For flexible-chain surfactants, the adsorption below the transition can lead to a two-dimensional solid condensed phase of surfactants with ordered, all-trans chains, whereas surfactants in the lower concentration 2-D phase above the transition may have disordered chains. As demonstrated below, a similar transition occurs for DHDHP extractants, which is then used to control the process of  $\text{Er}^{3+}$  extraction into dodecane by controlling the density and ordering of DHDHP extractants at the interface.

**Interfacial Tension from Samples without Er.** Figure 1 compares interfacial tension data obtained from a reference

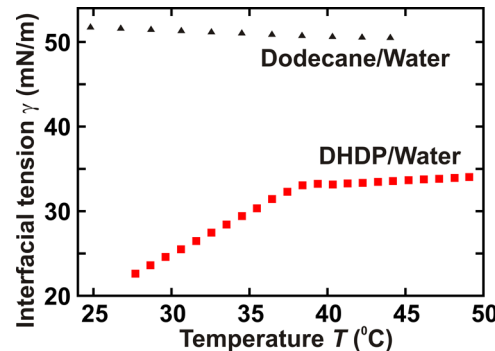


**Figure 1.** Variation of interfacial tension with temperature at the interfaces between pure water and pure dodecane ( $\blacktriangle$ ) and between pure water and  $10^{-4}$  M DHDHP in dodecane (red ■).

interface between pure water and pure dodecane and an interface between pure water and a dodecane solution of  $10^{-4}$  M DHDHP. The variation of interfacial tension with temperature characterizes an interface by providing a measurement of the interfacial excess entropy per unit area  $S_a^\sigma = -(d\gamma/dT)_{p,c}$  measured at fixed pressure and composition.<sup>22</sup> The slightly negative slope measured for the pure dodecane–water interface reveals the higher entropy ( $S_a^\sigma = 0.07 \text{ mJ/m}^2\text{K}$ ) of interfacial molecules and is typical of such an interface. Observed differences in both the interfacial tension at a given temperature and its temperature dependence for the sample to which  $10^{-4}$  M DHDHP has been added to the organic phase reveal that DHDHP has a marked impact on the interfacial excess entropy. The negative interfacial excess entropy,  $S_a^\sigma = -1.0 \text{ mJ/m}^2\text{K}$ , below the transition at  $T_0 = 38.2 \text{ }^\circ\text{C}$  is consistent with temperature effects involving molecular organization in the interfacial region.<sup>19,23,24</sup> The change in excess entropy to  $S_a^\sigma = -0.1 \text{ mJ/m}^2\text{K}$  above the transition reveals a much less ordered interface that could be the result of an order–disorder transition of DHDHP molecules at the interface, or it could be due to an adsorption/desorption process for which cooling through the transition brings DHDHP molecules to the interface and heating removes them. X-ray reflectivity and Brewster angle microscopy measurements discussed below demonstrate that both adsorption/desorption and chain ordering/disordering occur at the transition.

**Brewster Angle Microscopy of the Transition.** Figure 2 illustrates Brewster angle microscope images that demonstrate the presence of a bright homogeneous interface well below the phase transition and a dark homogeneous interface well above the transition, as well as the formation of bright domains close to the transition temperature. These images are consistent with

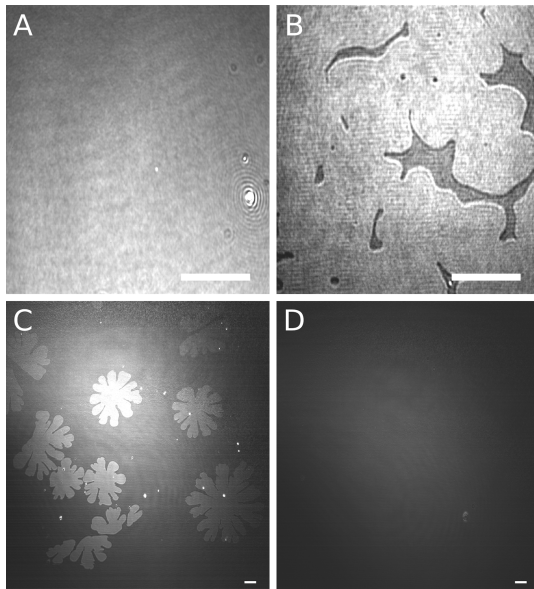


**Figure 2.** Brewster angle microscope images of an interface between pure water and  $10^{-4}$  M DHDP in dodecane at (A)  $T_0 - 3.8\text{ }^\circ\text{C}$ , (B)  $T_0 - 0.8\text{ }^\circ\text{C}$ , (C)  $T_0 + 0.1\text{ }^\circ\text{C}$ , and (D)  $T_0 + 1.7\text{ }^\circ\text{C}$ . Images A and B have a horizontal field of view of  $380\text{ }\mu\text{m}$ , and images C and D have a horizontal field of view of  $2.25\text{ mm}$ . The brightness in this series of images is a relative, not absolute, measure of optical contrast. Scale bars represent  $100\text{ }\mu\text{m}$ .

an adsorption transition that occurs as the temperature is lowered through the transition, but do not provide molecular-level structural information.

**X-ray Reflectivity from Samples without Er.** X-ray reflectivity is a technique for probing the electron density variation  $\rho(z)$  along the interfacial normal  $z$  but averaged over the  $x$ - $y$  plane of the interface.<sup>4</sup> Molecular organization at the interface is then determined by making a correspondence between the measured electron density and the known electron density of specific molecular arrangements. A schematic of the experimental sample is presented in Figure 3A along with the X-ray kinematics. X-ray reflectivity was measured as a function of the angle of incidence  $\alpha$ , which determines the wave vector transfer perpendicular to the interface  $Q_z = \vec{k}_{\text{out}} - \vec{k}_{\text{in}} = 2k_0 \sin \alpha$ , where  $k_0 = 2\pi/\lambda$  is the wavenumber (with X-ray wavelength  $\lambda = 0.61992\text{ \AA}$ ). Prior to X-ray reflectivity measurements, the sample was heated above the transition to  $45\text{ }^\circ\text{C}$ , then cooled to  $28\text{ }^\circ\text{C}$  to anneal interfacial inhomogeneities caused by the initial contact between solutions that occurs during sample preparation. Figure 3B shows the reflectivity data for the interface between pure water and  $10^{-4}$  M DHDP extractant in dodecane, above and below the observed transition temperature at  $38.2\text{ }^\circ\text{C}$ .

X-ray reflectivity data at  $28\text{ }^\circ\text{C}$  were fit to an electron density profile (Figure 3C) as described in Materials and Methods. Modeling the X-ray reflectivity data below the transition temperature with a single layer of DHDP molecules is consistent with the presence of a close-packed monolayer of DHDP molecules with nearly all-trans tailgroups at the dodecane–water interface, as shown in Figure 3D. A conventional two-slab electron density profile that represents DHDP head groups and tail groups by a separate slab was first used to fit the reflectivity data. It yielded a fit whose quality at large  $Q_z$  ( $>0.35\text{ \AA}^{-1}$ ) could be improved significantly by the addition of a thin ( $\sim 3\text{ \AA}$ ) slab that represents the terminal ends

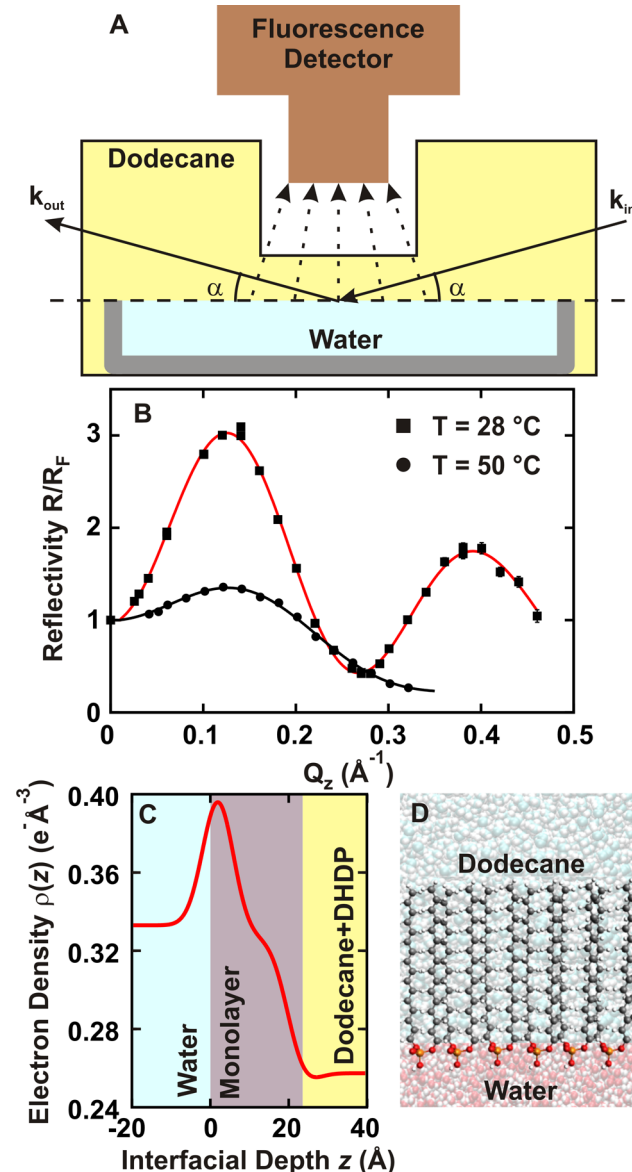


**Figure 3.** Experimental setup, data, and modeling for X-ray reflectivity measurements from the interface between pure water and  $10^{-4}$  M DHDP in dodecane. (A) Teflon sample cell contains the aqueous phase in a glass tray (gray) surrounded by dodecane. Kinematics of X-ray reflectivity:  $\vec{k}_{\text{in}}$ , incoming X-ray wave vector;  $\vec{k}_{\text{out}}$ , reflected wave vector, and angles of incidence and reflection,  $\alpha$ . Dashed arrows indicate fluorescence X-rays generated isotropically by the sample, which are measured by the fluorescence detector. (B) Measured X-ray reflectivity normalized to the calculated Fresnel reflectivity,  $R(Q_z)/R_F(Q_z)$ , from the interface between pure water and  $10^{-4}$  M DHDP in dodecane at  $28\text{ }^\circ\text{C}$  (■ with red line fit) and  $50\text{ }^\circ\text{C}$  (● with black line fit). Points at  $Q_z = 0$  are measured from transmission through the bulk organic phase. Solid line through the data at  $28\text{ }^\circ\text{C}$  is the best fit calculated from the electron density profile shown in (C), which is illustrated by the cartoon in (D).

of the tail groups (see parameters in Table 1). This additional slab, together with its lower electron density, implies either that the ends of the tail groups are disordered, as previously observed in long-chain alkanols at the water–hexane interface,<sup>23</sup> or that the electron density of the methyl end-group is lower than the rest of the tail group.<sup>25</sup> These measurements cannot distinguish between these two possibilities. The value of

**Table 1.** Best-Fit Parameters to the X-ray Reflectivity Data<sup>a</sup>

| aqueous phase                                  | $\sigma$ (Å)        | $d_1$ (Å)            | $\rho_1$ ( $e^-/\text{\AA}^3$ ) | $d_2$ (Å)            | $\rho_2$ ( $e^-/\text{\AA}^3$ ) | $d_3$ (Å)            | $\rho_3$ ( $e^-/\text{\AA}^3$ ) |
|--|---------------------|----------------------|---------------------------------|----------------------|---------------------------------|----------------------|---------------------------------|
| water (28 °C)                                  | $3.8^{+0.2}_{-0.4}$ | $4.1^{+2.9}_{-1.1}$  | $0.491^{+0.056}_{-0.066}$       | $16.5^{+0.9}_{-2.3}$ | $0.327^{+0.003}_{-0.003}$       | $3.0^{+3}_{-1}$      | $0.22^{+0.03}_{-0.02}$          |
| water (50 °C)                                  | $3.6^{+0.6}_{-0.4}$ | $3.6^{+1.9}_{-0.6}$  | $0.427^{+0.028}_{-0.040}$       | $11.3^{+0.7}_{-1.4}$ | $0.300^{+0.002}_{-0.004}$       | N/A                  | N/A                             |
| $5 \times 10^{-7}$ M ErBr <sub>3</sub> (28 °C) | $3.6^{+0.4}_{-0.3}$ | $18.9^{+0.8}_{-0.6}$ | $0.279^{+0.003}_{-0.003}$       | $8.5^{+3.9}_{-2.8}$  | $0.329^{+0.013}_{-0.008}$       | $18.5^{+2.1}_{-3.5}$ | $0.324^{+0.003}_{-0.003}$       |

<sup>a</sup>Fits to data from interfaces between  $10^{-4}$  M DHDP in dodecane and water (first and second rows) and the interface between  $10^{-4}$  M DHDP in dodecane and  $5 \times 10^{-7}$  M ErBr<sub>3</sub> in water (pH = 2.5, adjusted with HBr). The electron densities of the bulk aqueous and organic phases are 0.333 and  $0.2574 e^-/\text{\AA}^3$ , respectively, at 28 °C. The thicknesses of the 3 slabs ( $d_1, d_2, d_3$ ), the electron densities of the slabs ( $\rho_1, \rho_2, \rho_3$ ), and the interfacial roughness  $\sigma$  are fitting parameters for the 28 °C samples. The parameters  $\sigma, d_1, d_2, \rho_1$ , and  $\rho_2$  are fit to the 50 °C data. For the analysis of the water sample without ErBr<sub>3</sub>; slab 1 represents the interfacial region that includes head groups, and slabs 2 and 3 represent the region of tail groups. For the analysis of the ErBr<sub>3</sub> sample; slabs 1 and 3 represent tail groups, and slab 2 represents the headgroup region that also includes Er<sup>3+</sup> and water. Slab 1 is adjacent to the aqueous phase.

electron density over most of the tail group length,  $\rho_2 = 0.327 e^- \text{ \AA}^{-3}$ , demonstrates that the alkyl chains are essentially all-trans, except possibly for the terminal end.<sup>26</sup> The total chain length of 19.5 Å, given by the total thickness of the two slabs that represent the tail group, is slightly smaller than the length of an all-trans alkyl chain, given by  $L_{\text{trans}} = 15 \times 1.27 \text{ \AA}$  (C–C) + 1.5 Å (C–H) = 20.6 Å.<sup>26</sup> This difference may be due to gauche conformations near the methyl end of the tail groups, although a small tilt of the tail group cannot be excluded by these measurements.

Upon raising the temperature above the transition to 50 °C, the X-ray reflectivity data are greatly reduced in amplitude and represent an interface with a lower density of DHDP (Figure 3B), although the presence of a weak peak indicates that the DHDP density has not been reduced to zero. This is consistent with the reduction of interfacial tension below that of the pure dodecane–water interface (Figure 1) and the dark BAM image in Figure 3D. Table 1 lists the fit parameters that describe a dilute monolayer of DHDP molecules at the interface with an area/molecule  $A = 80^{+10}_{-6} \text{ \AA}^2$ , as compared to  $A = 42.7^{+2.2}_{-1.9} \text{ \AA}^2$  below the transition (see the Supporting Information for the calculation of  $A$ ). This shows that ~50% of DHDP molecules leave the interface when the sample temperature is raised through the transition. The fit parameters in Table 1 suggest a thin, disordered region of DHDP tail groups. The transition occurs between a low-temperature high-density monolayer of ordered DHDP molecules and a high-temperature low-density monolayer of disordered DHDP. Note that chain disordering alone cannot explain these data (see Figure S2 and accompanying text in the Supporting Information).

**Adsorption Transition in Samples with Er.** The behavior of interfacial tension upon addition of  $5 \times 10^{-7}$  M ErBr<sub>3</sub> in water (pH 2.5 adjusted with HBr) to the DHDP system indicates that a similar transition occurs when ErBr<sub>3</sub> is present at the acidic conditions commonly used for solvent extraction (Figure 4). The lower pH of this sample with ErBr<sub>3</sub> leads to a higher interfacial tension above the transition. This feature, along with the even weaker reflectivity peak above the transition (Figure S2 in the Supporting Information), indicates that more than 50% of DHDP molecules leave the interface upon heating above the transition. This suggests the possibility, supported by the experiments described below, that the adsorption transition at  $T_0 = 31.8$  °C can be used to control the process of Er<sup>3+</sup> extraction into dodecane by controlling the transport of DHDP extractants to and from the interface.

The difference between the heating (1, 3) and cooling (2, 4) curves in Figure 4 is attributable to the presence of ErBr<sub>3</sub> in the

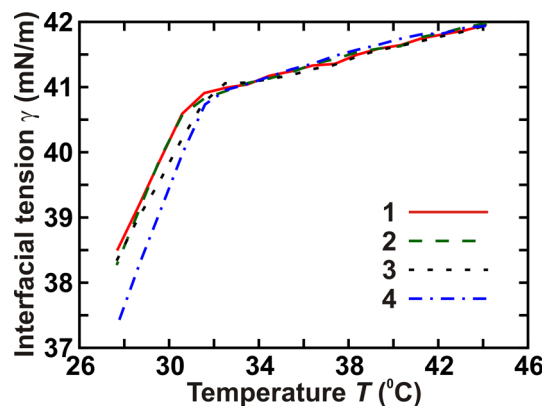


**Figure 4.** Interfacial tension for liquid–liquid interfaces prepared at 28–29 °C with pH 2.5 aqueous ErBr<sub>3</sub> solutions (curves 3 and 4) and without ErBr<sub>3</sub> (curves 1 and 2). Curve 1 (solid red) and curve 2 (long-dashed green) indicate reproducible heating (1) and cooling (2) curves for an interface between water (pH 2.5, adjusted with HBr) and  $1 \times 10^{-4}$  M DHDP in dodecane. Curve 3 (short-dashed black) and curve 4 (dash-dotted blue) are heating (3) and cooling (4) curves for an interface between  $5 \times 10^{-7}$  M ErBr<sub>3</sub> in water (pH 2.5, adjusted with HBr) and  $1 \times 10^{-4}$  M DHDP in dodecane. Temperature steps are 1 °C with equilibration at each temperature.

aqueous phase during the first heating curve (3). As shown later in this Article, erbium ions are extracted from the aqueous phase above the transition, so that cooling curve 4 does not reproduce the data below the transition temperature. Subsequent heating and cooling cycles will reproduce the cooling curve 4. The slopes below  $T_0$  are nearly the same for curves 1, 2, and 4, which is consistent with the extraction of Er ions during the high temperature part of curve 3. The interfacial excess entropies above the transition are  $S_a^\sigma = -0.085 \text{ mJ/m}^2 \cdot \text{K}$ , whereas the entropies below the transition are  $S_{a,1}^\sigma = -0.72 \text{ mJ/m}^2 \cdot \text{K}$ ,  $S_{a,2}^\sigma = -0.79 \text{ mJ/m}^2 \cdot \text{K}$ ,  $S_{a,3}^\sigma = -0.63 \text{ mJ/m}^2 \cdot \text{K}$ , and  $S_{a,4}^\sigma = -0.87 \text{ mJ/m}^2 \cdot \text{K}$ . Values of  $\Delta S_a^\sigma = S_{a,\text{above}}^\sigma - S_{a,\text{below}}^\sigma$  are slightly smaller than measurements on adsorption transitions and slightly larger than measurements on surface freezing transitions for alkanols of similar chain length.<sup>19,23,24</sup>

**Measurement of Interfacial Ion–Extractant Complexes.** Figure 5 illustrates representative X-ray reflectivity results from solutions containing Er<sup>3+</sup> that were prepared following a specific protocol designed to optimize the measurement of ion–extractant complexes formed during the process of extracting Er<sup>3+</sup> from the aqueous phase into the dodecane phase. The sample was prepared by adding a

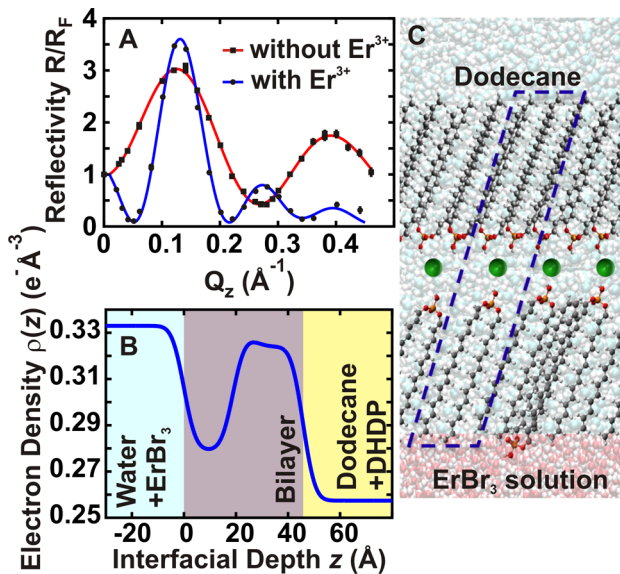


**Figure 5.** X-ray reflectivity results for samples containing Er. (A) Normalized X-ray reflectivity  $R(Q_z)/R_f(Q_z)$  from the interface between  $5 \times 10^{-7}$  M  $\text{ErBr}_3$  in water (pH 2.5 adjusted with HBr) and  $10^{-4}$  M DHDP in dodecane (● with blue line fit), and for comparison (previously shown in Figure 3), from the interface between pure water and  $10^{-4}$  M DHDP in dodecane (■ with red line fit), both at  $28^\circ\text{C}$ . Points at  $Q_z = 0$  are measured from transmission through the bulk organic phase. The blue line is the best fit calculated from the electron density profile shown in (B), which provides the basis for the inverted bilayer with  $\text{ErBr}_3$  illustrated in (C). The dashed box in (C) illustrates the ion-extractant complex – 3 DHDP molecules that coordinate with one  $\text{Er}^{3+}$ . The lower leaflet of DHDP molecules is loosely packed and/or slightly disordered (not shown in cartoon) with a density lower than that of the upper leaflet. Additional DHDP molecules instead of dodecane molecules may be mixed into the lower leaflet. One anchor molecule with its headgroup in the water is shown in the lower leaflet of the bilayer in (C); see Discussion.

dodecane solution of DHDP that had been heated to  $34^\circ\text{C}$  (above  $T_0 = 31.8^\circ\text{C}$ ) to an aqueous  $\text{ErBr}_3$  solution held in a sample thermostat kept at  $28^\circ\text{C}$ . This method allows extraction to occur for the short time (<15 min) that the interfacial temperature is above the transition temperature, then slows or arrests the extraction upon cooling the interfacial region below  $T_0$ , where a condensed interfacial phase is formed and characterized with X-rays. As described below, the condensed interfacial phase of ion-extractant complexes can be maintained for one or more days, but heating the sample above  $T_0$  for a couple of hours will extract  $\text{Er}^{3+}$  from the aqueous phase and produce the interfacial monolayer of DHDP previously observed in samples prepared with pure water.

X-ray reflectivity from this sample exhibits oscillations with about one-half the wavelength of those from the sample without  $\text{ErBr}_3$ , revealing an interfacial film in the presence of  $\text{Er}^{3+}$  that is about twice as thick as the monolayer observed in its absence (Figure 5A). A 3-slab model for the electron density profile in Figure 5B produces the best-fit parameters listed in Table 1. Models with fewer slabs cannot fit the data. The first and third slabs have similar thickness; each is slightly shorter than the all-trans length  $L_{\text{trans}}$ . The first slab (slab 1 in Table 1) is in contact with the aqueous phase at the bottom of the layer, and the third is in contact with the dodecane phase at the top of the layer. A thinner slab 2 is situated between these two slabs. On the basis of their electron density and thickness values, the

first and third slabs represent alkyl chains, while the second slab consists of the  $\text{Er}$ –headgroup complex and, possibly, water molecules.

The large electron density of the third slab,  $\rho_3 = 0.324 \pm 0.003 \text{ e}^-/\text{\AA}^3$ , is consistent with an upper leaflet of tail groups (in contact with dodecane) that is close-packed and essentially all-trans,<sup>26</sup> even though the thickness of this layer,  $d_3 = 18.5^{+2.1}_{-3.5} \text{ \AA}$ , is less than the all-trans length,  $20.6 \text{ \AA}$ , of the chain. Assuming that this is due primarily to chain tilting, the tilt angle from the interface normal can be calculated as  $\cos^{-1}(d_3/L_{\text{trans}}) = 26^\circ$ , similar to values commonly observed in close-packed crystals of alkanes.<sup>27</sup> The area  $A$  per DHDP molecule in the upper leaflet of the bilayer is then given by  $A = 2A_0L_{\text{trans}}/d_3 = 44^{+5}_{-4} \text{ \AA}^2$ , where  $A_0 = 19.8 \text{ \AA}^2$  is the cross-sectional area per alkyl chain in the all-trans state and the value of the upper error bar includes the effect of placing a sensible limit on the maximum tilt angle for DHDP in the upper leaflet (< $35^\circ$ ).<sup>26–28</sup> The lower layer of tail-groups (in contact with water) has a similar thickness of  $18.9^{+0.8}_{-0.6} \text{ \AA}$ , but a lower electron density,  $0.279 \pm 0.003 \text{ e}^- \text{ \AA}^{-3}$ , implying a larger surface area per DHDP, which could be the result of intermixing of dodecane into this region of the inverted bilayer, as illustrated in Figure 5C, or it could be due to the presence of gauche conformations in the alkyl chains of DHDP.

The thickness of the middle region of the inverted bilayer is  $d_2 = 8.5^{+3.9}_{-2.8} \text{ \AA}$ , and its average electron density is  $\rho_2 = 0.329^{+0.013}_{-0.008} \text{ e}^- \text{ \AA}^{-3}$ . Assuming that headgroups of DHDP,  $\text{Er}^{3+}$  ions, and water molecules are in the middle slab, the total number of electrons per lipid area in this slab is given by

$$d_2\rho_2 A = N_{\text{PO}_4^-} e_{\text{PO}_4^-} + N_{\text{Er}^{3+}} e_{\text{Er}^{3+}} + N_{\text{H}_2\text{O}} e_{\text{H}_2\text{O}} \quad (3)$$

where  $N$  and  $e$  represent the number of each species per surface area  $A$  and the number of electrons for each species. The inverted bilayer structure shown in Figure 5C, together with  $A = 44 \text{ \AA}^2$ , yields one  $\text{Er}^{3+}$  per  $88 \text{ \AA}^2$  with  $3.5^{+10.5}_{-3.5}$  water molecules. Note that the reflectivity measurements do not specifically probe the presence of water molecules, just their effect on the average electron density, which leads to large errors on their number in the headgroup region of the inverted bilayer. Similarly, reflectivity measurements do not specifically measure the presence of  $\text{Er}^{3+}$  ions. Therefore, the X-ray fluorescence measurements presented below, which are ion-specific, are required to present a unique characterization of the ion-extractant complexes that form the inverted bilayer.

The interfacial structure of an inverted bilayer, which places the lower leaflet of tail groups adjacent to water and has moved  $\text{Er}^{3+}$  ions into its shielded interior, is unexpected. However, the appearance of a minimum in the reflectivity just above the critical wave vector transfer  $Q_c \approx 0.01 \text{ \AA}^{-1}$  is a signature feature of an inverted bilayer that would not be observed for more conventional interfacial layers, such as a bilayer that has headgroups in contact with water and dodecane, or with monolayer, trilayer, and interfacial structures with more layers, as illustrated in Figure 6. The behavior of the X-ray reflectivity at low  $Q_z$  is most sensitive to the interference of X-rays reflected from the bottom and top of the interfacial layer,  $R/R_f \propto \Delta\rho_{\text{bottom}}\Delta\rho_{\text{top}} \cos(Q_z d)$ , where  $\Delta\rho_{\text{bottom}}$  is the electron density difference between the water phase and the bottom of the layer adjacent to water,  $\Delta\rho_{\text{top}}$  is the electron density difference between the top of the layer adjacent to dodecane and the dodecane phase, and  $d$  is the total layer thickness (see the Supporting Information for the full calculation). Because the differences  $\Delta\rho_{\text{bottom}}$  and  $\Delta\rho_{\text{top}}$  have the same sign for an

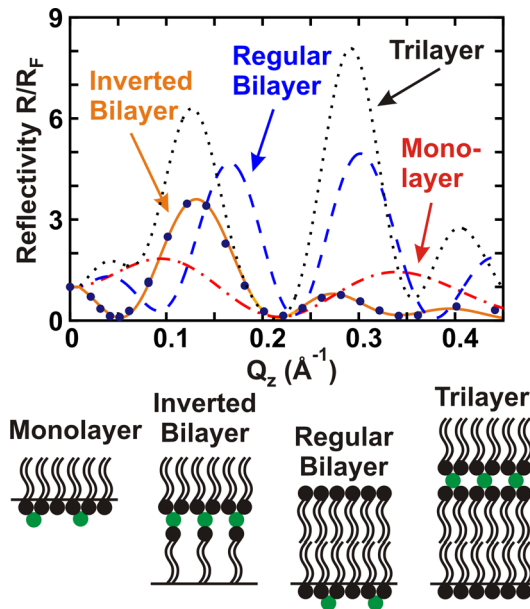


**Figure 6.** Normalized X-ray reflectivity  $R(Q_z)/R_F(Q_z)$  (dark blue ●) from an interface between a  $10^{-4}$  M dodecane solution of DHDP and a  $5 \times 10^{-7}$  M aqueous solution of  $\text{ErBr}_3$  ( $\text{pH} = 2.5$  adjusted with HBr) at  $28^\circ\text{C}$ . A cartoon of the structures used for the calculations is shown below, where green dots represent Er. Calculations of a typical monolayer (red dash-dotted line), regular bilayer (blue dashed line), trilayer (black dotted line), and the best fit from the inverted bilayer (orange solid line) are also illustrated. A regular bilayer or trilayer has the polar phosphate groups of the lowest leaflet of DHDP in water, similar to the arrangement of the monolayer shown in Figure 3D. It is seen that only the inverted bilayer structure can fit the low  $Q_z$  minimum in reflectivity. Interfacial structures with more layers of similar thickness would have shorter-period oscillations that would be inconsistent with the reflectivity data.

inverted bilayer,  $R/R_F \propto +\cos(Q_z d)$  and  $R/R_F$  is expected to decrease at low  $Q_z$ , as measured when the sample has  $\text{ErBr}_3$  (Figure 6). All of the other layer configurations illustrated in Figure 6 have  $\Delta\rho_{\text{bottom}}$  and  $\Delta\rho_{\text{top}}$  of opposite sign, so that  $R/R_F \propto -\cos(Q_z d)$  and  $R/R_F$  should increase at low  $Q_z$ . Note that  $\Delta\rho_{\text{bottom}}$  and  $\Delta\rho_{\text{top}}$  represent the primary electron density differences at the bottom and top of the interfacial layer. For instance, the small density depletion at the methyl end of an ordered tail group, similar to that observed for the monolayer in the system without Er (Table 1), has a negligible effect and does not alter these conclusions.

**Fluorescence Measurements.** X-ray fluorescence near total reflection (XFNTR) measurements are complementary to reflectivity measurements because they are element-specific and in this case can be used to determine the interfacial density of Er ions.<sup>15</sup> For values of wave-vector transfer  $Q_z$  smaller than the critical value ( $Q_z < Q_c \approx 0.01 \text{ \AA}^{-1}$ ), X-rays penetrate the interface evanescently for a few nanometers, and Er fluorescence is excited only from atoms very close to the interface. Even if X-rays penetrate much further into the lower phase (when  $Q_z > Q_c$ ), the fluorescence is measurable only if ions accumulate at the interface because of the low ion concentration in the bulk aqueous phase. Characteristic Er L shell fluorescence emission lines were measured from the inverted bilayer structure (Figure 7A), thus confirming an enhanced concentration of Er ions at the interface. Although  $\text{Br}^-$  fluorescence lines appear in the spectrum at higher energies as a result of  $\text{Br}^-$  in the bulk aqueous phase, our analysis shows

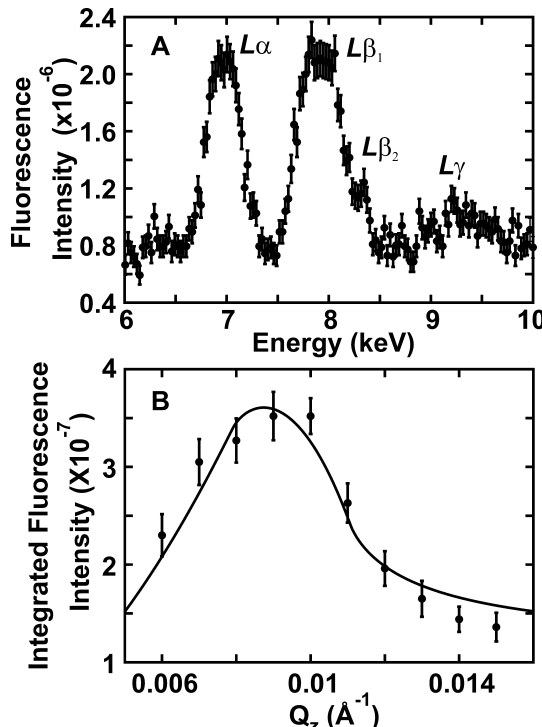


**Figure 7.** X-ray fluorescence data and analysis from an interface between  $10^{-4}$  M DHDP in dodecane and  $5 \times 10^{-7}$  M  $\text{ErBr}_3$  in water ( $\text{pH} = 2.5$ , adjusted with HBr) at  $28^\circ\text{C}$ . (A) X-ray fluorescence spectra of Er measured below the critical angle at  $Q_z = 0.008 \text{ \AA}^{-1}$  (X-ray penetration depth of  $170 \text{ \AA}$ ). (B) The integrated experimental fluorescence intensity measured as a function of  $Q_z$  near the critical angle for total reflection. The integrated intensity is determined by the product of the Er  $\text{L}\alpha$  emission peak intensity and peak width determined by fitting the peaks to a Gaussian function.

that the  $\text{Br}^-$  interfacial density is negligible (see Figure S3 and accompanying text in the Supporting Information).

The measured variation of fluorescence intensity with  $Q_z$  shown in Figure 7B is determined by the distribution of Er ions. The interfacial density of Er ions is given by  $I/\text{CTL}$ , where  $I$  is the interfacial term  $I_L$ , and  $C$  is the scale factor described in Materials and Methods,  $L$  is an integration over X-ray paths through the sample, and  $T$  is the Fresnel transmission coefficient.<sup>15</sup> Because the coefficient  $T$  has a sharp peak at the critical wave vector transfer  $Q_c$ , the rounded top in the experimental data (Figure 7B) implies that interfacial curvature cannot be ignored. The fit in Figure 7B models the interface as a spherical surface with radius of curvature of  $90 \pm 7 \text{ m}$ , as determined from a fit to the  $Q_z$ -dependence of  $\text{Br K}\alpha$  emission line data measured from the same sample (see the Supporting Information). The fit reveals that there is one Er ion per  $81^{+6}_{-4} \text{ \AA}^2$  of interface.

**Model of the Inverted Bilayer and Ion-Extractant Complexes.** The combined results from X-ray fluorescence and reflectivity measurements provide the basis for proposing the detailed model of the inverted bilayer illustrated in Figure 5C. The interfacial area of  $81^{+6}_{-4} \text{ \AA}^2$  per  $\text{Er}^{3+}$  ion from the fluorescence analysis, together with the extractant molecular area in the upper leaflet of  $44^{+5}_{-4} \text{ \AA}^2$  from the reflectivity, suggests that each  $\text{Er}^{3+}$  ion binds to two phosphate headgroups from the upper leaflet of the bilayer. Greater uncertainty exists for the number of DHDP per  $\text{Er}^{3+}$  in the lower leaflet of the bilayer because X-ray measurements cannot determine whether

additional DHDP chains or dodecane chains occupy the space beyond that required for one DHDP in the lower leaflet. Nevertheless, a model that includes more DHDP chains must also account for their accompanying head groups. Our data limit the fraction of head groups in direct contact with the aqueous phase to be small, ~10% (see the Supporting Information), so that most head groups will be located in the midregion of the inverted bilayer. On the one hand, the assumption that dodecane is mixed into the lower leaflet is consistent with one DHDP per  $\text{Er}^{3+}$  with  $3.5^{+10.5}_{-3.5}$  water molecules in the middle region containing head groups and  $\text{Er}^{3+}$ . On the other hand, the assumption that dodecane is absent in the lower leaflet is consistent with the presence of up to 1.8 DHDP per  $\text{Er}^{3+}$  in the lower leaflet, a number that takes into account the errors on the electron density and thickness of the lower leaflet and on the area per  $\text{Er}^{3+}$  from XFNTR measurements. Charge neutrality suggests that the additional fraction (<0.8) of a DHDP per  $\text{Er}^{3+}$  must be protonated and neutral because XFNTR results show that  $\text{Br}^-$  is absent from the bilayer. Because this assumption places more DHDP headgroups, say 0.8 per  $\text{Er}^{3+}$ , in the middle region of the bilayer, the number of water molecules in the middle headgroup region would be reduced from 3.5 to essentially zero.

For the various models that we examined, the simplest model of the ion-extractant complex that is consistent with both X-ray reflectivity and fluorescence data consists of three DHDP phosphate headgroups, two from the upper layer and one from the lower layer, coordinated to each  $\text{Er}^{3+}$  ion, as shown in the dashed box in Figure 5C. An important outcome of this interfacial structure, along with the absence of  $\text{Br}^-$  ions at the interface, is that it leads to local charge neutrality in the vicinity of each  $\text{Er}^{3+}$  ion, an intuitive attribute for a complex in a nonpolar solvent. Although our interfacial measurements are not consistent with the complexing of an average of two or four DHDP molecules per  $\text{Er}^{3+}$  ion, they cannot exclude the presence of an additional fraction up to 0.8 DHDP per  $\text{Er}^{3+}$  in the lower leaflet. This indicates that a fraction of  $\text{Er}^{3+}$  ions in the midregion of the inverted bilayer can be complexed to more than three DHDP molecules.

**Extraction of Er into the Dodecane Phase.** Several methods showed directly or indirectly that DHDP extracts Er from water into dodecane. First, inductively coupled plasma atomic emission spectroscopy (ICP-AES) measured the aqueous-phase Er concentration before and after heating the sample above the transition temperature  $T_0$ . A  $10^{-4}$  M DHDP solution in dodecane and a  $5 \times 10^{-6}$  M  $\text{ErBr}_3$  aqueous solution ( $\text{pH} = 2.5$  adjusted with HBr) of equal volumes were placed in contact in a glass dish held at  $55^\circ\text{C}$  for 24 h. After this time, the ICP-AES measurement determined that the Er concentration in the aqueous phase had been reduced from  $5 \times 10^{-6}$  M to less than  $10^{-6}$  M, the limit of experimental resolution, thus providing a direct measurement of Er ion extraction from the aqueous phase. The initial concentration of  $5 \times 10^{-6}$  M  $\text{ErBr}_3$  chosen for the ICP-AES measurements was higher than that used for X-ray measurements because of the ICP-AES instrumental resolution.

**X-ray Reflectivity and Fluorescence.** X-ray reflectivity measurements provide indirect evidence that Er ions are extracted from the water phase. After heating a dodecane ( $10^{-4}$  M DHDP)-water ( $5 \times 10^{-7}$  M  $\text{ErBr}_3$ ,  $\text{pH} = 2.5$ ) sample above the transition temperature  $T_0$  to  $40^\circ\text{C}$  for 2 h, X-ray reflectivity measurements demonstrate that this sample interface, upon cooling below  $T_0$  to  $28^\circ\text{C}$ , contains only a monolayer of

DHDP, as observed by the form of the data in Figure 8, as well as by detailed analysis (not shown). The presence of the

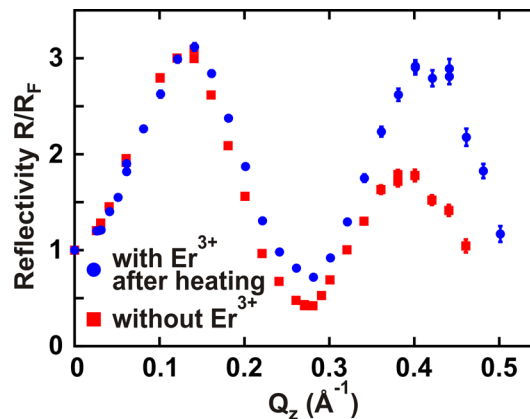


**Figure 8.** Normalized X-ray reflectivity  $R(Q_z)/R_F(Q_z)$  from the interface between  $10^{-4}$  M DHDP in dodecane and pure water (red ■) and an interface between  $10^{-4}$  M DHDP in dodecane and  $10^{-7}$  M  $\text{ErBr}_3$  in water ( $\text{pH} = 2.5$  adjusted with HBr; blue ●). The red ■ and blue ● illustrate measurements carried out at  $28^\circ\text{C}$  after heating the samples to  $45$  and  $40^\circ\text{C}$ , respectively, then cooling to  $28^\circ\text{C}$ . The low  $Q_z$  behavior and the similarity of the two sets of data show that the sample with  $\text{ErBr}_3$ , after heating and cooling, had a monolayer at the interface, as did the sample without erbium.

DHDP monolayer, as previously observed for samples prepared without  $\text{Er}^{3+}$  ions in the aqueous phase, as well as the absence of the inverted bilayer suggest that  $\text{Er}^{3+}$  ions have been extracted from the water. Further evidence that heating to  $40^\circ\text{C}$  for 2 h extracts  $\text{Er}^{3+}$  was provided by fluorescence measurements from a similar sample, but with  $\text{ErCl}_3$  substituting for  $\text{ErBr}_3$ , that demonstrated the disappearance of Er fluorescence peaks along with the appearance of the DHDP monolayer.

**XAFS Determines the Extracted Er Coordination.** XAFS measurements demonstrate directly that Er ion–DHDP extractant complexes are observed in the dodecane phase after heating samples above the transition temperature  $T_0$ . XAFS data were measured by transmitting X-rays through bulk phases taken from separately prepared samples (described in Materials and Methods) to determine the Er–O and Er–P coordination in the Er–DHDP complex extracted into the organic phase. The normalized Er L<sub>3</sub>-edge XAFS measurements of the aqueous reference solution and of the organic phases with extractant complexes are illustrated in Figure 9A. The shapes and positions of the peaks for the aqueous reference sample (labeled 22 mM) differ from the data measured from the three organic phases. Background-subtracted  $k^3\chi(k)$  EXAFS (extended XAFS, Figure 9C) for the aqueous and organic samples are also different, where  $k$  is the wavenumber of the photoejected electrons and  $\chi(k)$  is the EXAFS fine structure function.<sup>29</sup> Data from the aqueous reference sample appear as a single damped sinusoid, whereas the other three data sets provide evidence for multiple sinusoidal components. Despite lower quality data at large  $k$  for the lowest concentration 0.1 mM sample, all three organic samples have a very similar overall shape, implying that the Er–DHDP coordination has negligible dependence on the initial Er concentration. The Fourier transform data of the  $k^3\chi(k)$  EXAFS for all four data sets (Figure 9D) display a prominent peak at  $1.6$ – $1.9$  Å (uncorrected for phase shift) that is associated with back-

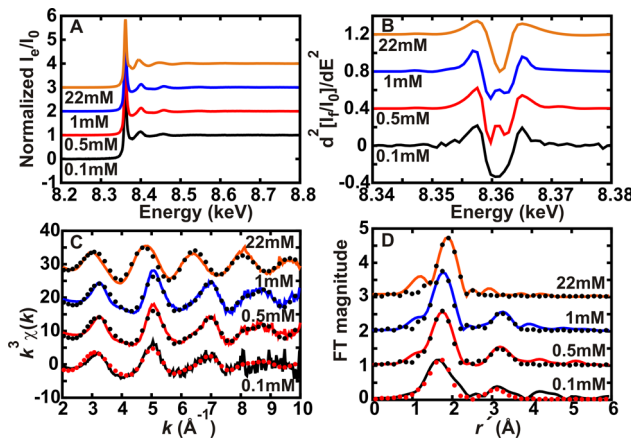


**Figure 9.** XAFS data and analysis. (A) Normalized Er  $L_3$ -edge XAFS data for the Er-DHDP complex in dodecane prepared by extracting  $\text{Er}^{3+}$  from aqueous solutions ( $\text{pH} = 2.5$ , adjusted with  $\text{HBr}$ ) with three different starting concentrations (0.1, 0.5, and 1 mM  $\text{ErBr}_3$ , see labels in figures) into dodecane solutions with three different DHDP concentrations (respectively, 1, 5, and 10 mM), as well as XAFS data from a 22 mM  $\text{ErBr}_3$  aqueous solution reference sample. (B) Second differential of the XANES (X-ray absorption near edge structure) data. (C) The  $k^3$ -weighted EXAFS obtained from experiment (solid lines) as compared to the fits (dots). (D) The corresponding Fourier transform of the data in (C), uncorrected for phase shifts, from experiment (solid lines) and fits (dots).

scattering from the innermost O atoms about Er. However, only the Fourier transform data for the organic samples exhibit a second peak, attributable to a second sphere Er–P correlation.

One-shell (Er–O) and two-shell (Er–O and Er–P) analyses were carried out to model the  $k^3\chi(k)$  EXAFS data for the aqueous and organic samples, respectively. The best-fit results are shown in Figure 9C,D with fitting parameters listed in Table 2. The result from the aqueous sample indicates that

**Table 2. EXAFS Best-Fit Parameters<sup>a</sup>**

| sample         | atom | $r$ (Å)   | CN       | $\sigma_{\text{DW}}^2$ (Å $^2$ ) | $\Delta E$ (eV) |
|----------------|------|-----------|----------|----------------------------------|-----------------|
| 22 mM aqueous  | O    | 2.336(12) | 7.8(9)   | 0.008(3)                         | -3.8(1.2)       |
| 1 mM organic   | O    | 2.218(9)  | 6.4(6)   | 0.008(3)                         | -3.9(1.2)       |
|                | P    | 3.733(18) | 3.9(9)   |                                  |                 |
| 0.5 mM organic | O    | 2.213(12) | 6.7(9)   | 0.009(3)                         | -4.7(1.2)       |
|                | P    | 3.716(21) | 4.4(1.2) |                                  |                 |
| 0.1 mM organic | O    | 2.204(27) | 7.4(2.1) | 0.015(3)                         | -7.9(2.7)       |
|                | P    | 3.70(6)   | 4.2(2.7) |                                  |                 |

<sup>a</sup>Interatomic distances ( $r$ ), coordination number (CN), Debye–Waller factors ( $\sigma_{\text{DW}}^2$ ), and energy threshold values ( $\Delta E$ ) from the fits shown in Figure 9C,D. Values shown in parentheses are 3 times the estimated standard deviations on the smallest digits.

7.8(9) oxygen atoms are in the first coordination shell at 2.336(12) Å, in excellent agreement with previous high-energy X-ray scattering results.<sup>12</sup> The organic-sample results show that each  $\text{Er}^{3+}$  ion is 6-fold coordinated with O atoms; these originate from DHDP ligands and water molecules. Although the coordination number (CN) of oxygen from the 0.1 mM sample appears as  $7.4 \pm 2.1$ , all three samples yield a similar Er–O distance (2.20–2.22 Å), consistent with literature values for the mean Er–O bond distance of 2.23 Å for CN = 6 and substantially shorter than literature values for CN = 7 (2.285 Å)

and CN = 8 (2.334 Å).<sup>30</sup> Moreover, two valleys in the second differential data (Figure 9B), although not obvious for the 0.1 mM sample, are another indicator of 6-fold-oxygen coordination of  $\text{Er}^{3+}$ , as was previously observed in EXAFS measurements on  $\text{Er}_2\text{O}_3$  and  $\text{Na}_3\text{ErSi}_3\text{O}_9$ .<sup>31</sup>

Analysis of the second coordination shell yields 3.70–3.73 Å for the Er–P distance and 3.9–4.4 for the P coordination number (Table 2). The Er–P correlation originates from the coordination of DHDP to Er through the O atoms of DHDP (Figure 10). The experimental distance is significantly larger

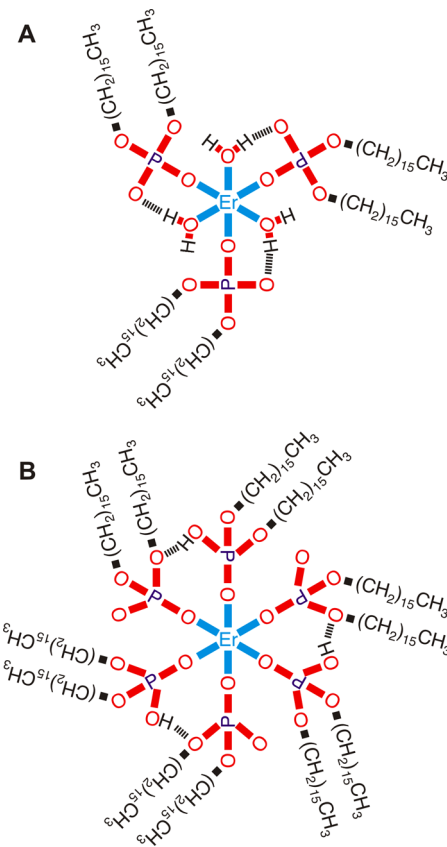


**Figure 10.** Schematic of structures proposed for  $\text{Er}^{3+}$  complex formed upon extraction with DHDP in the bulk dodecane phase, including (A) 3 DHDP and 3  $\text{H}_2\text{O}$ , and (B) 6 DHDP and 0  $\text{H}_2\text{O}$  in the  $\text{Er}^{3+}$  coordination. The measured average P coordination number suggests that the structure in (A) is the dominant structure in bulk dodecane. The structure in (A) is also consistent with X-ray reflectivity and fluorescence measurements of ion-extractant complexes in the interfacial inverted bilayer.

than literature values (3.1 Å) for bidentate coordination ( $\text{Er}-\text{O}_2\text{PO}_2$ ), but close to literature values (3.5–3.6 Å) for monodentate coordination ( $\text{Er}-\text{OPO}_3$ ), implying that each  $\text{PO}_4$  group contributes only one O atom to the Er first coordination shell.<sup>32,33</sup> Therefore, there must be a few  $\text{H}_2\text{O}$  molecules in the first shell to compensate for the difference between the Er–O and Er–P coordination numbers. Overall, the extracted Er–DHDP complex coordination in the organic phase is in agreement with the interfacial inverted bilayer structure, which contains an average of ~3  $\text{PO}_4$  groups and  $3.5^{+10.5}_{-3.5}$   $\text{H}_2\text{O}$  for each  $\text{Er}^{3+}$ .

Although the EXAFS data on the coordination numbers have large error bars on the average P coordination, for example,  $3.9 \pm 0.9$ , it is similar to the average value of 3–3.8 P atoms per

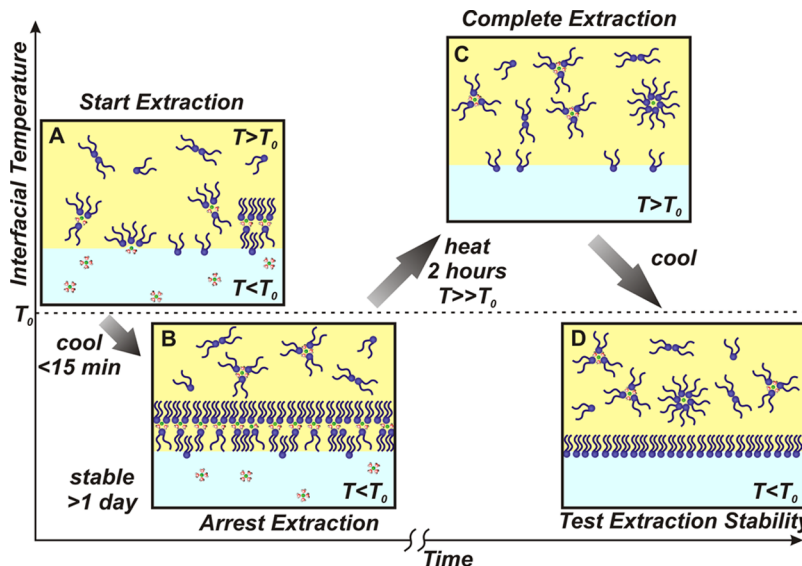


**Figure 11.** Cartoon of a temperature sequence used to study solvent extraction of  $\text{Er}^{3+}$  ions from the lower aqueous phase to the upper oil (dodecane) phase containing DHDP extractants. (A) An oil phase at  $T > T_0$  placed on top of a thermostated aqueous phase held at  $T < T_0$  initiates solvent extraction in the interfacial region, which stays above  $T_0$  for a short time. (B) Subsequent cooling below the adsorption transition temperature  $T_0$  arrests the extraction, producing a condensed layer of interfacial ion-extractant complexes that is studied with X-rays for up to  $\sim 24$  h. (C) Heating above the transition allows the extraction process to proceed to completion within a couple of hours. (D) Recooling through  $T_0$  shows that the bulk ion-extractant complexes are stable in the oil phase and do not precipitate onto the interface.

$\text{Er}^{3+}$  ion observed for the interfacial inverted bilayer. Other studies of the extracted complex in the bulk organic phase have observed the two structures illustrated in Figure 10, for which additional DHDP molecules from the bulk dodecane replace  $\text{H}_2\text{O}$  molecules (see Figure 10B).<sup>10</sup> A combination of these two structures is consistent with the average P coordination of  $3.9 \pm 0.9$ . These considerations imply that the majority of ion-extractant complexes in the bulk organic phase have the coordination illustrated in Figure 10A that is consistent with the complexes observed in the interfacial inverted bilayer.

#### 4. DISCUSSION

**Interfacial Ion-Extractant Complexes.** During solvent extraction, ions in water are transported across the oil–water interface to be enclosed in reverse micelles of extractants in the oil phase. Some authors, considering the amphiphilic nature of extractants, have proposed that the formation of extractant monolayers at the oil–water interface underlies this transport process, but no studies of interfacial structures that form during transport have been reported previously.<sup>34–37</sup> Under the conditions of our experiments, a sample in the midst of extracting metal ions from an aqueous to an organic phase is cooled below an adsorption phase transition (Figure 11A). This arrests the extraction, thereby immobilizing supramolecular ion-extractant complexes at the oil–water interface (Figure 11B). The extractants form a condensed interfacial layer, an inverted bilayer, which was characterized on the molecular scale with X-ray reflectivity and fluorescence. The interfacial complex consists of an average of  $\sim 3$  DHDP extractants whose head groups surround a central  $\text{Er}^{3+}$  ion and  $\sim 3$  water molecules, along with extractant tail groups that extend outward.

An inverted bilayer presents a counterintuitive interfacial arrangement of extractants, in which polar head groups are separated from the aqueous phase, and hydrophobic end groups are placed in contact with water. Although an inverted bilayer has not been observed previously at the liquid–liquid

interface, it has been reported for arachidic acid surfactant Langmuir monolayers compressed into a nonequilibrium collapsed state on the surface of water,<sup>38</sup> as well as in equilibrium behenic acid Langmuir–Blodgett films on a hydrophobic solid substrate.<sup>39</sup> The stability of inverted bilayers has been previously rationalized on the basis of the free energy gain from strong electrostatic interactions of the multivalent ions, as well as enhanced van der Waals interactions (per interfacial area) between alkyl chains, which dominate the energetic penalty of breaking hydrogen bonds between headgroups and water, as well as other lower energy interactions such as the penalty for placing alkyl chains in contact with water.<sup>39,40</sup> The arrangement of molecules and ions within the inverted bilayer optimizes the coordination of  $\text{Er}^{3+}$  ions to DHDP head groups over that achieved in a monolayer arrangement where multiple DHDP head groups have to crowd together to coordinate with ions in the water.

It is expected that the free energy could be lowered further if the inverted bilayer broke free of the interface and diffused into the bulk organic phase, thus placing the terminal ends of the alkyl chains of the lower leaflet in contact with dodecane instead of water. This happens for  $T > T_0$  to realize the extraction of  $\text{Er}^{3+}$  ions (Figure 11A,C). We speculate that a contributing factor that stabilizes the inverted bilayer below the transition is a small fraction of DHDP molecules adsorbed headfirst onto the water, which anchor the bilayer (Figure 11B). Analysis of the data shown in Figure 5 indicates that up to 10% of the interfacial area can be occupied by DHDP anchors. An inhomogeneous interface consisting of inverted bilayer combined with anchoring molecules is consistent with the dynamics of ion-extractant complex formation discussed below.

**Ion-Extractant Complexes Are Formed at the Interface.** These experiments did not probe the interfacial molecular dynamics of the process that forms interfacial ion-extractant complexes out of individual extractants and a

hydrated  $\text{Er}^{3+}$  ion. Nevertheless, evidence was presented that ion-extractant complexes are formed at the interface, not in the bulk phase. The negligible solubility of, on the one hand, DHDHP in a pH 2.5 aqueous phase and, on the other hand,  $\text{Er}^{3+}$  ions in dodecane suggests that these components cannot enter the unfavorable phase as isolated entities to subsequently form ion-extractant complexes. Our experiments show in addition that ion-extractant complexes observed at the interface upon cooling through the adsorption transition are not the result of precipitation of complexes from the organic phase. To demonstrate this, a standard sample was prepared with  $5 \times 10^{-7}$  M  $\text{ErBr}_3$  in water (pH = 2.5) and  $10^{-4}$  M DHDHP in dodecane, which exhibited an inverted bilayer at the interface (Figure 11B). The sample was heated to 40 °C for 2 h, during which time  $\text{Er}^{3+}$  ions were essentially fully extracted from the aqueous phase into the organic phase (Figure 11C). At this stage, the sample has ion-extractant complexes in the bulk organic phase, but essentially no  $\text{Er}^{3+}$  in water. Subsequent cooling of the sample to below the adsorption temperature  $T_0$  did not precipitate ion-extractant complexes onto the interface to reform the inverted bilayer. Instead, DHDHP monolayers were observed (Figures 8 and 11D), which were likely formed from DHDHP molecules in the bulk dodecane that were not complexed with Er ions. Consistent with this, X-ray fluorescence indicated the absence of  $\text{Er}^{3+}$  ions at the interface. At the end of a similar experiment with  $\text{ErCl}_3$  in place of  $\text{ErBr}_3$ , spontaneous formation of an inverted bilayer was subsequently observed when additional  $\text{ErCl}_3$  was injected into the aqueous phase. These results provide strong evidence that Er-DHDHP complexes are not formed in the bulk and, therefore, are formed at the interface.

X-ray reflectivity studies of the aqueous solution-vapor interface of  $\text{ErCl}_3$  solutions previously demonstrated a propensity for hydrated  $\text{Er}^{3+}$  ions to approach the interface.<sup>13</sup> It is plausible that  $\text{Er}^{3+}$  ion-extractant complexes are formed by the approach of 3 DHDHP extractants from the oil side of the interface that are attracted by an  $\text{Er}^{3+}$  ion on the water side of the interface (Figure 11A). A subsequent dynamic instability of the interface in the vicinity of the ion and extractants leads to the formation of the ion-extractant complex at the interface, which optimizes the interaction of DHDHP extractants and  $\text{Er}^{3+}$ . In our experiments, we arrested this process in the midst of extraction and discovered that ion-extractant complexes are stabilized in a condensed interfacial phase. The inverted bilayer phase characterized earlier in this Article in molecular detail was obtained following a specific thermal protocol, in which a thermostated aqueous phase was held at a fixed temperature a few degrees below the adsorption temperature  $T_0$ , while an oil phase whose temperature was above  $T_0$  was poured on top (Figure 11A).

#### Thermal Effect on Interfacial Molecular Ordering.

Prior to our understanding the role of the thermal protocol in preparing samples, experiments provided irreproducible X-ray reflectivity patterns generally suggestive of extractant ordering at the interface that is inhomogeneous within the interfacial plane, as measured by scanning an X-ray beam with a footprint of  $\sim 1$  mm across the sample interface. Nevertheless, the low  $Q_z$  feature in the X-ray reflectivity of an inverted bilayer was observed, although generally with less pronounced minima and maxima than in Figure 5A. In retrospect, it is likely that these samples contained a mixture of inverted bilayer and monolayer at the interface because extraction was not occurring uniformly throughout the interface when the condensed interfacial phase

was formed. Unfortunately, it is difficult to quantitatively analyze the X-ray reflectivity of inhomogeneous interfaces.<sup>4</sup> The observation of such variability is not entirely unexpected because it has been previously demonstrated that the history and preconditioning of solvent-extraction systems can play a significant role in the kinetics and efficacy of their separations, for reasons not understood.<sup>41</sup>

Given the expected dynamical nature of the process of forming interfacial ion-extractant complexes, it is not surprising that the previously described thermal protocol did not always produce exactly the same reflectivity curve, although we always observed an inverted bilayer or features of a more complex inhomogeneous interface. Also, different thermal protocols produced different results. For instance, measurements of samples prepared below the transition temperature  $T_0$ , then briefly heated and cooled back through  $T_0$ , sometimes exhibit an inverted bilayer whose lower leaflet has a higher density than the inverted bilayer described previously (Figure 12; see the Supporting Information for detailed analysis).

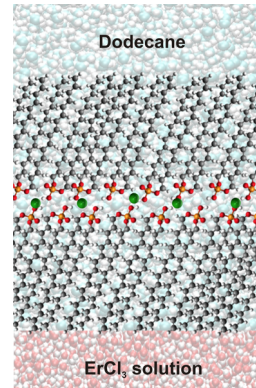


**Figure 12.** Alternative structure of inverted bilayer of ion-extractant complexes occasionally observed in place of the structure described in Figure 5.

Because our analysis of this alternate structure is based entirely upon X-ray reflectivity data, without the advantage of XFNR data, there is some uncertainty in the  $\text{Er}^{3+}$  interfacial density and, consequently, in the underlying structure of ion-extractant complexes, which could have 3 or 4 DHDHP molecules per  $\text{Er}^{3+}$ . Although this is similar to the coordination shown for the ion-extractant complex in Figure 5C, these two forms of the inverted bilayer have characteristic and distinctly different X-ray reflectivity curves (see Figure S4, Table S1, and text in the Supporting Information). To summarize our experience with this system, an interfacial inverted DHDHP bilayer has been observed for samples prepared and kept below the transition temperature, as well as for any thermal history for which the sample is above the transition temperature for a period of time on the order of minutes.

Variability was also observed in the results of interfacial tension measurements when preparing samples below the transition temperature. For this reason, it is not possible to make a correspondence between interfacial excess entropies measured by interfacial tension and the interfacial molecular order observed in X-ray studies. Future experiments are planned to address this issue by fabricating a sample cell that allows for concurrent measurements of interfacial tension, X-ray reflectivity, and X-ray fluorescence.

**Similarity of Interfacial and Extracted Ion-Extractant Complexes.** Upon heating the sample above the phase transition, the interfacial bilayer dissolves into the organic phase and metal ions are extracted (Figure 11C). XAFS measurements demonstrated that the coordination of Er ions, water, and DHDP extractants in the extracted complexes is consistent with the structure observed at the interface. It is possible that interfacial ion-extractant complexes pick up additional DHDP molecules upon moving into the bulk that alter the coordination, as suggested by Figure 10B, or to form larger micelles containing more than 6 DHDP molecules. If these additional DHDP molecules were positioned further from the Er ion than about 5 Å, perhaps in a large micelle, then XAFS experiments would not be sensitive to them, and other techniques would be required to detect them. The totality of experiments described in this Article suggests a causal connection between ion-extractant complexes formed at the interface and those extracted into the bulk oil (Figure 11). The interfacial ion-extractant complexes are an intermediate state in the solvent extraction process.

**Outlook.** Common industrial organo-phosphorus extractants<sup>3</sup> are composed of shorter alkyl tails than DHDP and are, therefore, expected to have adsorption transitions at much lower temperatures, below that of industrial extraction conditions. Our experiments utilized the adsorption transition as a device to immobilize the interfacial ion-extractant complex so that it could be characterized with X-rays. Nevertheless, the knowledge that supramolecular ion-extractant complexes are formed directly at the interface during the extraction process, and the structure of these complexes, is relevant to understanding and optimizing the kinetics of commercial extractant systems.<sup>41</sup> These experiments suggest that further understanding can be gained by exploring other chemical systems to see if similar interfacial complexes are observed, as well as by studies that probe the dynamic formation of the complexes.

## 5. CONCLUSION

Interfaces between dodecane solutions of a DHDP extractant and aqueous solutions of  $\text{ErBr}_3$  or  $\text{ErCl}_3$  were studied to probe the process of solvent extraction of  $\text{Er}^{3+}$  ions from water to dodecane. Temperature variations in the vicinity of an adsorption phase transition, in which extractants are adsorbed to the oil-water interface, provide a level of control to essentially stop and start the extraction process. Supramolecular ion-extractant complexes formed at the interface condense into an inverted bilayer when extraction is stopped before completion. X-ray reflectivity and fluorescence measurements demonstrate that the ion-extractant complex consists of 3 DHDP extractants and 3 water molecules per  $\text{Er}^{3+}$  with measurement errors allowing for an average of at most 3.8 DHDP in a complex. After extraction was completed, X-ray absorption spectroscopy of the bulk oil phase demonstrated that the  $\text{Er}^{3+}$  ion coordination to water and extractant molecules in bulk ion-extractant complexes is consistent with the structure of interfacial ion-extractant complexes. Our observations provide evidence for a route to metal ion extraction that starts with hydrated ions in the aqueous phase,<sup>12</sup> which are then transformed at the aqueous-organic interface into supramolecular ion-extractant complexes that form the basis for the complex extractant ordering previously observed in bulk organic phases associated with extraction processes.<sup>10,11</sup> More generally, this work demonstrates the possibility of using X-rays to characterize the structure of

supramolecular interfacial complexes that are important for ion transport and other dynamic processes at liquid-liquid interfaces.

## ■ ASSOCIATED CONTENT

### S Supporting Information

XFNTR data from a reference sample (Figure S1), analysis of area per molecule for samples without erbium, an analysis of high temperature X-ray reflectivity data (Figure S2 and text), a calculation demonstrating the form of the low  $Q_z$  reflectivity from an inverted bilayer, XFNTR data and analysis for  $\text{Br}^-$  (Figure S3 and text), and a detailed description of the alternate inverted bilayer structure (Figure S4, Table S1, and text). This material is available free of charge via the Internet at <http://pubs.acs.org>.

## ■ AUTHOR INFORMATION

### Corresponding Authors

\*E-mail: schloss@uic.edu.  
\*E-mail: ls@anl.gov.  
\*E-mail: weibu@uic.edu.

### Present Address

<sup>1</sup>BSRF, Institute of High Energy Physics, Chinese Academy of Sciences, Beijing 100049, China.

### Notes

The authors declare no competing financial interest.

## ■ ACKNOWLEDGMENTS

This work was supported by the U.S. DOE, OBES, Chemical Sciences, Geosciences, and Biosciences Division under contract no. DE-AC02-06CH11357. The Advanced Photon Source, OBES, Materials Sciences is supported under DE-AC02-06CH11357. M.L.S. also acknowledges support from NSF-CHE-0910825. ChemMatCARS (Sector 15 of the Advanced Photon Source) is supported by NSF-CHE-1346572. Sungsik Lee assisted with XAFS data measurements at 12-BM-B of the Advanced Photon Source, John Regalbuto's group assisted with ICP-AES measurements, and Thomas Bsaibes and Glenn Hanlon assisted with the BAM measurements.

## ■ ABBREVIATIONS

DHDP, dihexadecyl phosphate; XAFS, X-ray absorption fine structure; XFNTR, X-ray fluorescence near total reflection

## ■ REFERENCES

- (1) Gouaux, E.; MacKinnon, R. Principles of Selective Ion Transport in Channels and Pumps. *Science* **2005**, *310*, 1461–1465.
- (2) Buffle, J.; Parthasarathy, N.; Djane, N. K.; Matthiasson, L. Permeation Liquid Membranes for Field Analysis and Speciation of Trace Compounds in Waters. *IUPAC Ser. Anal. Phys. Chem. Environ. Syst.* **2000**, *6*, 407–493.
- (3) *Ion Exchange and Solvent Extraction: A Series of Advances*; Moyer, B. A., Ed.; CRC Press: Boca Raton, FL, 2010; Vol. 19.
- (4) Pershan, P. S.; Schlossman, M. L. *Liquid Surfaces and Interfaces: Synchrotron X-Ray Methods*; Cambridge University Press: Cambridge, 2012.
- (5) Tasker, P. A.; Plieger, P. G.; West, L. C. Metal Complexes for Hydrometallurgy and Extraction. In *Comprehensive Coordination Chemistry II: From Biology to Nanotechnology*; McCleverty, J. A., Meyer, T. J., Eds.; Elsevier: Oxford, 2004; Vol. 9, pp 759–808.
- (6) Stevens, G. W.; Perera, J. M.; Greiser, F. Interfacial Aspects of Metal Ion Extraction in Liquid-Liquid Systems. *Rev. Chem. Eng.* **2001**, *17*, 87–110.

- (7) Tondre, C.; Hebrant, M.; Watarai, H. Rate of Interfacial Reactions Compared to Bulk Reactions in Liquid-Liquid and Micellar Processes: An Attempt to Clarify a Confusing Situation. *J. Colloid Interface Sci.* **2001**, *243*, 1–10.
- (8) Benay, G.; Wipff, G. Liquid-Liquid Extraction of Uranyl by TBP: The TBP and Ions Models and Related Interfacial Features Revisited by MD and PMF Simulations. *J. Phys. Chem. B* **2014**, *118*, 3133–3149.
- (9) Marcus, Y.; Kertes, A. S. *Ion Exchange and Solvent Extraction of Metal Complexes*; Wiley-Interscience: London, 1969.
- (10) Gannaz, B.; Antonio, M. R.; Chiarizia, R.; Hill, C.; Cote, G. Structural Study of Trivalent Lanthanide and Actinide Complexes Formed Upon Solvent Extraction. *Dalton Trans.* **2006**, *38*, 4553–4562.
- (11) Ellis, R. J.; Audras, M.; Antonio, M. R. Mesoscopic Aspects of Phase Transitions in a Solvent Extraction System. *Langmuir* **2012**, *28*, 15498–15504.
- (12) Soderholm, L.; Skanthakumar, S.; Wilson, R. E. Structures and Energetics of Erbium Chloride Complexes in Aqueous Solution. *J. Phys. Chem. A* **2009**, *113*, 6391–6397.
- (13) Luo, G.; Bu, W.; Mihaylov, M.; Kuzmenko, I.; Schlossman, M. L.; Soderholm, L. X-Ray Reflectivity Reveals a Non-Monotonic Ion-Density Profile Perpendicular to the Surface of  $\text{ErCl}_3$  Aqueous Solutions. *J. Phys. Chem. C* **2013**, *117*, 19082–19090.
- (14) Gaonkar, A. G.; Neuman, R. D. Interfacial Activity, Extractant Selectivity, and Reversed Micellization in Hydrometallurgical Liquid-Liquid-Extraction Systems. *J. Colloid Interface Sci.* **1987**, *119*, 251–261.
- (15) Bu, W.; Hou, B.; Mihaylov, M.; Kuzmenko, I.; Lin, B.; Meron, M.; Soderholm, L.; Luo, G.; Schlossman, M. L. X-Ray Fluorescence from a Model Liquid/Liquid Solvent Extraction System. *J. Appl. Phys.* **2011**, *110*, 102214.
- (16) Uredat, S.; Findenegg, G. H. Domain Formation in Gibbs Monolayers at Oil/Water Interfaces Studied by Brewster Angle Microscopy. *Langmuir* **1999**, *15*, 1108.
- (17) Zhang, Z.; Mitrinovic, D. M.; Williams, S. M.; Huang, Z.; Schlossman, M. L. X-Ray Scattering from Monolayers of  $\text{F}-(\text{CF}_2)_{10}(\text{CH}_2)_2\text{OH}$  at the Water-(Hexane Solution) and Water-Vapor Interfaces. *J. Chem. Phys.* **1999**, *110*, 7421–7432.
- (18) Parratt, L. G. Surface Studies of Solids by Total Reflection of X-Rays. *Phys. Rev.* **1954**, *95*, 359–369.
- (19) Matubayasi, N.; Motomura, K.; Aratono, M.; Matuura, R. Thermodynamic Study on the Adsorption of 1-Octadecanol at Hexane/Water Interface. *Bull. Chem. Soc. Jpn.* **1978**, *51*, 2800.
- (20) Takiue, T.; Uemura, A.; Ikeda, N.; Motomura, K.; Aratono, M. Thermodynamic Study on Phase Transition in Adsorbed Film of Fluoroalkanol at the Hexane/Water Interface. 3. Temperature Effect on the Adsorption of 1,1,2,2-Tetrahydroheptadecafluorodecanol. *J. Phys. Chem. B* **1998**, *102*, 3724.
- (21) Schlossman, M. L.; Tikhonov, A. M. Molecular Ordering and Phase Behavior of Surfactants at Water-Oil Interfaces as Probed by X-Ray Surface Scattering. *Annu. Rev. Phys. Chem.* **2008**, *59*, 153–177.
- (22) Lyklema, J. *Fundamentals of Interface and Colloid Science III. Liquid-Fluid Interfaces*; Academic Press: San Diego, CA, 2000.
- (23) Tikhonov, A. M.; Pingali, S. V.; Schlossman, M. L. Molecular Ordering and Phase Transitions in Alkanol Monolayers at the Water-Hexane Interface. *J. Chem. Phys.* **2004**, *120*, 11822–11838.
- (24) Gang, O.; Wu, X. Z.; Ocko, B. M.; Sirota, E. B.; Deutsch, M. Surface Freezing in Chain Molecules: II. Neat and Hydrated Alcohols. *Phys. Rev. E* **1998**, *58*, 6086.
- (25) Ocko, B. M.; Dhinojwala, A.; Daillant, J. Comment on “How Water Meets a Hydrophobic Surface”. *Phys. Rev. Lett.* **2008**, *101*, 039601.
- (26) Small, D. M. *The Physical Chemistry of Lipids*; Plenum: New York, 1986.
- (27) Kitaigorodskii, A. I. *Organic Chemical Crystallography*; Consultants Bureau: New York, 1961.
- (28) Bu, W.; Vaknin, D.; Travesset, A. How Accurate Is Poisson-Boltzmann Theory for Monovalent Ions near Highly Charged Interfaces? *Langmuir* **2006**, *22*, 5673–5681.
- (29) Bunker, G. *Introduction to XAFS: A Practical Guide to X-Ray Absorption Fine Structure Spectroscopy*; Cambridge University Press: Cambridge, 2010.
- (30) Shannon, R. D. Revised Effective Ionic Radii and Systematic Studies of Interatomic Distances in Halides and Chalcogenides. *Acta Crystallogr., Sect. A* **1976**, *32*, 751.
- (31) Antonio, M. R.; Soderholm, L.; Ellison, A. J. G. Local Environments of Erbium and Lutetium in Sodium Silicate Glasses. *J. Alloys Compd.* **1997**, *250*, 536.
- (32) Wang, C.-M.; Wu, Y.-Y.; Hou, C.-H.; Chen, C.-C.; Lii, K.-H. Synthesis, Characterization, and Properties of Organically Tempered Lanthanide Oxalatophosphates with a Three-Dimensional Honeycomb Structure:  $(\text{H}_4\text{APPiP})[\text{Ln}_3(\text{C}_2\text{O}_4)_{5.5}(\text{H}_2\text{PO}_4)_2]\cdot\text{SH}_2\text{O}$  ( $\text{Ln}=\text{Er}, \text{Lu}$ , APPiP=1,4-Bis(3-aminopropyl)piperazine). *Inorg. Chem.* **2009**, *48*, 1519–1523.
- (33) Capitelli, F.; Bali, B. E.; Essehlri, R.; Lachkar, M.; Silva, I. D. New Hybrid Diphosphates  $\text{Ln}_2(\text{NH}_2(\text{CH}_2)_2\text{NH}_2)(\text{HP}_2\text{O}_7)_2\cdot 4\text{H}_2\text{O}$  ( $\text{Ln}=\text{Eu}, \text{Tb}, \text{Er}$ ): Synthesis, Single Crystal and Powder X-Ray Crystal Structure. *Z. Kristallogr.* **2006**, *221*, 788–794.
- (34) Hunt, E. C. The Interaction of Alkyl Phosphate Monolayers with Metal Ions. *J. Colloid Interface Sci.* **1969**, *29*, 105–115.
- (35) Szymanski, J. Kinetics and Interfacial Phenomena. *Solvent Extr. Ion Exch.* **2000**, *18*, 729–751.
- (36) Watarai, H.; Tsukahara, S.; Nagatani, H.; Ohashi, A. Interfacial Nanochemistry in Liquid-Liquid Extraction Systems. *Bull. Chem. Soc. Jpn.* **2003**, *76*, 1471–1492.
- (37) Testard, F.; Berthon, L.; Zemb, T. Liquid-Liquid Extraction: An Adsorption Isotherm at Divided Interface? *C. R. Chimie* **2007**, *10*, 1034–1041.
- (38) Vaknin, D.; Bu, W.; Satija, S. K.; Travesset, A. Ordering by Collapse: Formation of Bilayer and Trilayer Crystals by Folding Langmuir Monolayers. *Langmuir* **2007**, *23*, 1888.
- (39) Chevalier, N. R.; Chevallard, C.; Guenoun, P. Monovalent Cations Trigger Inverted Bilayer Formation of Surfactant Films. *Langmuir* **2010**, *26*, 15824–15829.
- (40) Lorenz, C. D.; Travesset, A. Atomistic Simulations of Langmuir Monolayer Collapse. *Langmuir* **2006**, *22*, 10016–10024.
- (41) Danesi, P. R.; Chiarizia, R. The Kinetics of Metal Solvent Extraction. *Crit. Rev. Anal. Chem.* **1980**, *10*, 1–126.